EarthArXiv Preprint Cover Sheet

Preprint title

Direct requested-time modelling of space-time fractional seismic attenuation on fixed operators

Authors

Ning Hu, Shuqun Li, Chengtao Huang, and Chuyang Hu

Affiliations

Ning Hu - School of Mechanical Engineering, Hangzhou Dianzi University, Hangzhou, China

Shuqun Li - School of Mathematics and Physics, Xi'an Jiaotong-Liverpool University, Suzhou, China

Chengtao Huang - School of Mechanical Engineering, Hangzhou Dianzi University, Hangzhou, China

Chuyang Hu - Department of Computer Science and Engineering, University of California, Santa Cruz, CA, USA

Corresponding author

Ning Hu, jluhooning@163.com

Version note

Direct requested-time modelling of space–time fractional seismic attenuation on fixed operators

Ning Hu[1,*], Shuqun Li[2], Chengtao Huang[1], Chuyang Hu[3]

[1] School of Mechanical Engineering, Hangzhou Dianzi University, Hangzhou, China

[2] School of Mathematics and Physics, Xi'an Jiaotong-Liverpool University, Suzhou, China

[3] Department of Computer Science and Engineering, University of California, Santa Cruz, CA 95064, USA

[*]Corresponding author: N. Hu, jluhooning@163.com.

Email addresses: Shuqun.Li24@student.xjtlu.edu.cn (S. Li); 25010330@hdu.edu.cn (C. Huang); chu207@ucsc.edu (C. Hu)

Abstract

Space–time fractional attenuation models represent dissipative memory and effective non-local dispersion in seismic wave propagation, but Caputo history marching is expensive when only selected receiver–time responses are required. Matrix Mittag–Leffler representations are classical; their use as a costed fixed-model response-query workflow for seismic attenuation is less developed. We formulate the space–time Mittag–Leffler eigen-evaluator (ST–MLEE) for a fixed positive self-adjoint semidiscrete seismic operator A_β, evaluating selected data as $d_r(t) = r^T E_\alpha(-t^\alpha A_\beta)b$ instead of advancing through all preceding time levels. Modal implementations reuse the eigensystem across times, receivers and dense source weights. Standard sparse Lanczos projection is cheaper for large operators, but its basis is source-dependent. The comparison is reported through q_*, ρ_t and ρ_r, which measure setup amortisation, requested-time sparsity and receiver sparsity. Same-equation L1/Grunwald–Letnikov history solvers validate the receiver traces within the 1.5% waveform tolerance on matched two-dimensional and controlled three-dimensional tests. On the largest irregular operator, a source-perturbation scan places the first single-vector Lanczos reuse failure at $\eta_b = 0.015$. Smooth variable-order matrices can be queried in the same fixed-operator form, whereas sharp geological contacts and PML-type absorbing boundaries require separate in-

terface or non-self-adjoint matrix-function treatments. For repeated fixed-operator queries with $q \geq q_*$ and sparse output fractions $\rho_t, \rho_r \ll 1$, matrix-function evaluation can bypass full Caputo time stepping while preserving matched waveform accuracy.

Key words: Seismic attenuation; Wave propagation; Fractional wave equation; Numerical modelling; Computational seismology.

1 Introduction

Attenuation in the Earth is commonly summarised by a quality factor Q that is nearly independent of frequency over the seismic band, the usual constant-Q approximation (Kjartansson, 1979; McDonal et al., 1958). Reproducing constant-Q attenuation together with its causal velocity dispersion has motivated a long line of rheological and fractional models. Standard time-domain viscoelasticity represents attenuation by a sum of relaxation mechanisms (generalised standard linear solid), which approximates constant-Q over a band at the cost of auxiliary memory variables (Carcione, 2014; Robertsson et al., 1994; Blanch et al., 1995). Space–time fractional wave equations instead represent power-law attenuation and dispersion with a Caputo time derivative of order α and a fractional spatial Laplacian of order β (Chen & Holm, 2004; Treeby & Cox, 2010; Zhu & Carcione, 2014; Caputo & Mainardi, 1971). The spatial order should be read as an effective non-local propagation parameter: the fractional Laplacian is a non-local operator whose value depends on the field over a spatial neighbourhood rather than only on local derivatives (Kwaśnicki, 2017), and in attenuation models it has been used to encode power-law dispersion associated with complex, heterogeneous media (Chen & Holm, 2004; Treeby & Cox, 2010).

Intrinsic dissipation and scattering by unresolved heterogeneity both contribute to band-limited attenuation and velocity dispersion in seismic data (Aki & Richards, 1980; Müller et al., 2010; Sato et al., 2012). In the model used below, α represents Caputo memory and intrinsic loss, whereas β represents effective spatial nonlocality and dispersion away from the $\beta = 2$ reference. We use β as an effective nonlocal-dispersion coordinate, without assuming a specific fractal closure.

Caputo history evaluation constitutes the principal computational bottleneck. Direct Caputo time discretisations retain a growing memory, giving $O(N_t)$ stored states and $O(N_t^2)$ work in an unaccelerated convolution (Lubich, 1986; Yuan & Agrawal, 2002). Once a spatial order varies, the phrase "variable-order fractional Laplacian" also no longer identifies a unique continuous or discrete operator. Seismic variable-space-order finite-difference and pseudospectral formulations already exist (Mu et al., 2021, 2022). We prescribe a positive self-adjoint semidiscrete spatial matrix and evaluate selected receiver-time responses for that fixed operator.

For a fixed Earth model in this sense, the requested datum has the form

$$d_r(t) = r^T E_\alpha(-t^\alpha A_\beta)b.$$

Once the spatial operator is assembled, the Caputo history need not be retained for every requested output. A dense modal representation or a source-dependent Krylov projection can evaluate selected times as matrix-function queries. Key application scenarios include receiver-time diagnostics, dense source-weight sweeps, fixed-model uncertainty tests and benchmark generation, where the same operator is queried repeatedly.

Classical modal solutions (Mainardi, 2010; Bazhlekova, 2001) and Krylov/rational matrix-function methods (Moret & Novati, 2011; Moret, 2015; Garrappa et al., 2015; Danczul et al., 2023) provide the numerical tools. We quantify how their setup costs and reuse limits shift when outputs are restricted to selected receiver-time queries rather than complete histories. We compare dense modal and source-dependent Lanczos routes through the measured break-even count q_*, validate receiver traces against independent same-equation L1 and Grunwald–Letnikov history solvers, and use source perturbations on an irregular heterogeneous operator to quantify the limits of standard single-vector Lanczos reuse.

2 Constant order: model and corrected dispersion relation

We take the constant-Q space–time fractional wave equation

$$^{C}D_t^\alpha u(\mathbf{x},t) + \kappa_{\alpha\beta}(-\Delta)^{\beta/2}u(\mathbf{x},t) = f(\mathbf{x},t), \qquad 1 < \alpha \le 2, \;\; 0 < \beta \le 2, \;\; \alpha+\beta > 2, \tag{1}$$

where $^{C}D_t^\alpha$ is the Caputo derivative of order α,

$$^{C}D_t^\alpha u(t) = \frac{1}{\Gamma(2-\alpha)} \int_0^t \frac{u''(\tau)}{(t-\tau)^{\alpha-1}}\,\mathrm{d}\tau, \qquad 1 < \alpha < 2, \tag{2}$$

and $(-\Delta)^{\beta/2}$ is the (spectral) fractional Laplacian, defined through the Dirichlet eigenbasis of $-\Delta$. The coefficient $\kappa_{\alpha\beta}$ has units $L^\beta T^{-\alpha}$, so the Caputo term and the spatial term have matching dimensions. In the classical limit $\alpha = \beta = 2$, $\kappa_{22} = c_0^2$ and (1) reduces to the standard wave equation. The companion WKB manuscript (Hu et al., 2025) writes the same coefficient dimensionlessly as $c^2(\mathbf{x})$ after nondimensionalisation by a reference time T_0 and length L_0;

	$\beta = 2$ (local space)	$\beta < 2$ (spatially non-local)
$\alpha = 2$	classical lossless wave	conservative anomalous spatial dispersion
$1 < \alpha < 2$	temporal-memory attenuation	attenuation plus non-local dispersion

Table 1: Reference limits defined by the temporal order α and spatial order β.

the two coincide once scales are fixed, $\kappa_{\alpha\beta} = c^2 L_0^\beta T_0^{-\alpha}$. All numerical examples are non-dimensionalised before evaluation. A typical seismic normalization is to choose $T_0 = 1/f_0$ and $L_0 = v_0 T_0$; for $f_0 = 10$ Hz and $v_0 = 3000$ m s^{-1}, this gives $T_0 = 0.1$ s and $L_0 = 300$ m, so the code evaluates ωT_0 and $|\mathbf{k}|L_0$. Unless a dimensional velocity model is specified, the experiments use the corresponding dimensionless coefficient and retain the notation $\kappa_{\alpha\beta}$ after this scaling. The differential equation can be studied on a wider parameter domain; the additional condition $\alpha + \beta > 2$ is imposed here only for the selected forward, non-amplifying wavenumber branch. For $1 < \alpha < 2$ it gives $0 < \theta < \pi/2$ and hence $k_R > 0$, $k_I > 0$, whereas $\alpha = 2$ is the lossless boundary with $\theta = 0$ and $k_I = 0$.

2.1 Reference limits of the two-order model

Table 1 records the limiting cases of the two-order model. The observables are not orthogonal because both orders enter the wavenumber relation.

2.2 Plane-wave analysis

Seek a plane-wave solution $u = \exp[\mathrm{i}(\mathbf{k} \cdot \mathbf{x} - \omega t)]$ of the homogeneous equation. We use the symbol correspondence for the Caputo derivative of a steady-state (single-frequency) time-harmonic factor: in the sense of the principal (Fourier) symbol of ${}^C D_t^\alpha$ for $\omega \neq 0$, the factor $e^{-\mathrm{i}\omega t}$ contributes $(-\mathrm{i}\omega)^\alpha e^{-\mathrm{i}\omega t}$. This is the standard steady-state/harmonic-response identity used throughout the fractional constant-Q literature (e.g. Chen & Holm, 2004; Treeby & Cox, 2010), not a claim about the transient (initial-value) Caputo operator, whose action on $e^{-\mathrm{i}\omega t}$ differs by initial-condition (edge) terms that decay and do not affect the steady-state dispersion relation used below. With this understanding, $(-\Delta)^{\beta/2}$ contributes $|\mathbf{k}|^\beta$. The dispersion relation is therefore

$$(-\mathrm{i}\omega)^\alpha + \kappa_{\alpha\beta}|\mathbf{k}|^\beta = 0, \qquad \Longrightarrow \qquad |\mathbf{k}| = \left(\frac{(-\mathrm{i}\omega)^\alpha}{-\kappa_{\alpha\beta}}\right)^{1/\beta}. \tag{3}$$

For $\omega > 0$, evaluating the principal branch $(-\mathrm{i}\omega)^\alpha = \omega^\alpha e^{-\mathrm{i}\pi\alpha/2}$ gives the complex wavenumber modulus and phase

$$k = \left(\frac{\omega^\alpha}{\kappa_{\alpha\beta}}\right)^{1/\beta} \exp\left[\frac{\mathrm{i}\pi}{\beta}\left(1 - \frac{\alpha}{2}\right)\right] \Big(\text{taking the root with } k_R > 0\Big), \tag{4}$$

where we choose $\arg(-\kappa_{\alpha\beta}) = -\pi$ for $\kappa_{\alpha\beta} > 0$. Thus the quotient in (3) has argument $-\pi\alpha/2 - (-\pi) = \pi(1 - \alpha/2)$, and its selected β-th root has the phase angle

$$\theta = \frac{\pi}{\beta}\left(1 - \frac{\alpha}{2}\right) = \frac{\pi(2-\alpha)}{2\beta}.$$

Splitting $k = k_R + \mathrm{i}k_I = |k|(\cos\theta + \mathrm{i}\sin\theta)$,

$$k_R = |k|\cos\theta, \qquad k_I = |k|\sin\theta, \qquad |k| = \left(\frac{\omega^\alpha}{\kappa_{\alpha\beta}}\right)^{1/\beta}. \tag{5}$$

We use the propagation quality-factor convention common in wavenumber-domain constant-Q modelling,

$$Q_{\text{prop}}^{-1} := 2\,\frac{k_I}{k_R} = 2\tan\theta, \qquad \theta = \frac{\pi(2-\alpha)}{2\beta}, \tag{6}$$

which is *independent of* ω—the constant-Q property—because the phase angle θ does not depend on frequency. A modulus- or energy-based definition formed from k^2 would instead give

$$Q_{\text{en}}^{-1} := \frac{\mathrm{Im}(k^2)}{\mathrm{Re}(k^2)} = \tan(2\theta) = \frac{2\tan\theta}{1 - \tan^2\theta}.$$

The two conventions agree to leading order in the high-Q limit $\tan\theta \ll 1$. Their difference is second order in $\tan\theta$, becoming visible only for strong attenuation. All Q values reported below use the propagation convention (6); low-Q cases should therefore be interpreted under this propagation definition rather than as energy-Q estimates. The phase velocity is

$$v_p = \frac{\omega}{k_R} = \frac{\omega}{\cos\theta}\left(\frac{\kappa_{\alpha\beta}}{\omega^\alpha}\right)^{1/\beta} = \frac{\kappa_{\alpha\beta}^{1/\beta}}{\cos\theta}\,\omega^{1-\alpha/\beta} \propto \omega^\gamma, \qquad \gamma = 1 - \frac{\alpha}{\beta}, \tag{7}$$

so the dispersion is a power law with index γ. Collecting (6) and (7) gives the *corrected* constant-Q relations

$$\boxed{Q_{\text{prop}}^{-1} = 2\tan\theta, \quad \theta = \frac{\pi(2-\alpha)}{2\beta}, \qquad \gamma = 1 - \frac{\alpha}{\beta}, \quad v_p \propto \omega^\gamma.} \tag{8}$$

The constant-Q relations (8) couple attenuation and dispersion through the β-th root of the complex wavenumber. The real self-adjoint spatial operator is non-dissipative by itself, but β still changes both the attenuation angle θ and the velocity-dispersion index $\gamma = 1 - \alpha/\beta$. Two limits check the algebra: at $\alpha = \beta = 2$, $\theta = 0$ so $Q^{-1} = 0$ and $\gamma = 0$—the loss-free, non-dispersive classical wave; and for a fixed β, decreasing α from 2 increases θ and hence the attenuation, while the dispersion index $\gamma = 1-\alpha/\beta$ measures departure from the dispersion-free line $\alpha = \beta$. Some presentations of the analogous constant-order relation omit the $1/\beta$ factor in the attenuation angle (implicitly $\beta = 2$); the explicit $1/\beta$ in (8) is essential once β is allowed to vary, since it is precisely what couples θ to the spatial order and enables the dual-observable identifiability used below.

2.3 Attenuation–dispersion interpretation of α and β

The reference case $\beta = 2$ gives a constant-Q medium whose causal dispersion is asymptotically consistent with Kjartansson's law in the high-Q limit. Departures from $\beta = 2$ represent departures from that attenuation–dispersion locking. At a fixed attenuation angle, changing β changes $\gamma = 1-\alpha/\beta$. Thus Q and broadband phase-velocity dispersion together identify (α, β), whereas Q alone leaves a one-parameter ambiguity (Figure 2).

Field and core observations show that attenuation and dispersion are not controlled by a single number. In the borehole/core dataset of Sams et al. (1997), the reported P-wave velocity changes by about 30 per cent across measurement bands and the intrinsic Q_P is strongly frequency dependent. These data motivate a two-order effective description in which β is a macroscopic fitting coordinate for nonlocal dispersion, not a direct measurement of a specific fractal or scattering microstructure. The same-equation tests below validate the fixed-operator evaluator.

Spatial variation of $\beta(\mathbf{x})$ is introduced after a concrete semidiscrete self-adjoint operator has been specified (§5). Supplementary Material S2 contains the field-data, joint variable-order, relaxation-order and scattering-origin diagnostics.

3 Requested-response Mittag–Leffler evaluator

3.1 Modal Mittag-Leffler representation

Let (λ_n, ϕ_n) be the Dirichlet eigenpairs of $-\Delta$ on the domain Ω, and set $\mu_n = \kappa_{\alpha\beta}\lambda_n^{\beta/2}$ so that $(-\Delta)^{\beta/2}\phi_n = \lambda_n^{\beta/2}\phi_n$. Projecting (1) onto ϕ_n and writing $U_n(t) = \langle u(\cdot,t), \phi_n\rangle$ reduces it to a scalar Caputo equation per mode,

$$ {}^{C}D_t^{\alpha} U_n + \mu_n U_n = F_n(t), \qquad U_n(0) = \langle u_0, \phi_n\rangle, \;\; U_n'(0) = \langle u_1, \phi_n\rangle, \tag{9} $$

whose solution is given in closed form by the Mittag-Leffler function $E_{\alpha,\beta}(z) = \sum_{k\ge 0} z^k/\Gamma(\alpha k+\beta)$. For a rest start ($u_1 = 0,\ f = 0$),

$$u(\mathbf{x}, t) = \sum_n \langle u_0, \phi_n \rangle\, E_\alpha(-\mu_n t^\alpha)\, \phi_n(\mathbf{x}), \tag{10}$$

with the velocity and source contributions added through the standard $t\,E_{\alpha,2}$ and Duhamel ($t^{\alpha-1}E_{\alpha,\alpha}$) terms. This modal formula defines the space–time Mittag–Leffler eigen-evaluator (ST–MLEE). The field at any requested t is evaluated directly from the modal factors, without time stepping, stored history or a CFL restriction. Memory is $O(N_x N_{\mathrm{mode}})$ for the eigenvectors. After setup, the temporal part of each requested output is independent of history depth: modal weighting and receiver projection scale with N_{mode}, not with the number of preceding levels N_t that a Caputo history scheme would have traversed.

Because modal evaluation relies on the spectral decomposition of a fixed semidiscrete operator A_β, spatial updates to $\beta(\mathbf{x})$, velocity structure, mesh or boundary realization alter the eigenbasis and require recomputing the representation. Variable $\alpha(\mathbf{x})$ does not commute with the modal projection and is routed to the Laplace–Talbot solver described in the Supplementary Material.

The history-depth-independent scaling applies to the *temporal* query evaluation after setup. End-to-end cost also includes setup and projection work. Obtaining (λ_n, ϕ_n) is a one-off cost that is reported with the benchmark. It is analytic for the Fourier/sine eigenbases used in the homogeneous and layered or velocity-heterogeneous experiments below. For a general heterogeneous self-adjoint operator $\mathcal{A} = -\nabla\cdot(c^2\nabla)$ without a closed-form eigenbasis (Section 4, "Heterogeneous models"), a numerical partial eigendecomposition costs $O(N_x^3)$ dense or $O(N_{\mathrm{mode}}\, N_x^2 \log N_x)$ with a Lanczos/Krylov solver for N_{mode} retained modes. A Krylov subspace approximation of the matrix Mittag–Leffler action (Hochbruck & Lubich, 1997; Higham, 2008) avoids forming the dense eigendecomposition but still incurs this setup cost.

The resulting cost comparison has two parts. History-dependent time marching costs $O(N_x N_t^2)$ in the unaccelerated convolution and does not require an eigendecomposition. ST–MLEE costs $O(N_{\mathrm{mode}} N_x^2 \log N_x) + O(N_{\mathrm{mode}})$ per query during a reusable query set. Dense or analytic eigenbases can be reused for many source weights, receivers and output times. A standard Lanczos matrix-action basis is generated from one starting source vector and is reused only across requested output times and receivers for that source. Operator-changing parameter-search workflows must rebuild the representation. On a one-shot large heterogeneous model with no closed-form eigenbasis, the setup cost can dominate. Figure 4 reports the accuracy/cost benchmark on a domain where the eigenbasis is analytic, so the eigendecomposition cost is zero.

The break-even condition is defined at matched accuracy. Let T_{setup} be the one-off eigendecomposition or Krylov-basis construction cost. Let T_{hist} be the per-query cost of a history-dependent solver that meets the same waveform tolerance as the cached modal or projected ST–MLEE evaluation. If T_{cached} is the per-query cached cost, the number of repeated forward queries needed to amortise the setup is

$$q_* = \left\lceil \frac{T_{\text{setup}}}{T_{\text{hist}} - T_{\text{cached}}} \right\rceil, \qquad T_{\text{hist}} > T_{\text{cached}}. \tag{11}$$

For $q < q_*$, setup dominates and time marching may be preferable. For $q \geq q_*$, the repeated queries amortise the fixed representation. On heterogeneous operators, T_{setup} includes the partial eigensolve or Krylov-basis construction, not only scalar Mittag–Leffler evaluation. Matched-accuracy comparisons use baselines that satisfy the same receiver-waveform tolerance. Any velocity, density, order, mesh, source-vector or boundary update that changes the representation resets the setup cost. We also report the requested-time fraction

$$\rho_t = \frac{N_q}{N_t}, \tag{12}$$

where N_t is the number of time levels required to span the recording interval by time marching and N_q is the number of output times actually queried. The response-query approach is most natural when $\rho_t \ll 1$. When only receiver traces are required, the companion reporting quantity is

$$\rho_r = \frac{N_r}{N_{\text{dof}}}, \tag{13}$$

quantifying output spatial sparsity relative to the discrete wavefield. Figure 3 reports the measured crossover for the low-setup analytic-basis benchmark. Equation (11) is recomputed for each mesh, tolerance and hardware setting.

Reuse depends on both the operator and the starting vector used to build the representation. Each benchmark reports the operator definition, self-adjointness, T_{setup}, T_{hist}, T_{cached}, q_*, ρ_t and ρ_r when receiver-only outputs are used. If the operator, source vector, boundary realization, mesh or order field changes between queries, the reuse counter is reset. The dense analytic-basis tests below are low-setup reuse cases; the irregular-grid Lanczos test is a single-source sparse matrix-action case.

On the 14,598-cell irregular operator, standard Lanczos reuse is sensitive to the starting source vector. Algebraically, the Lanczos basis spans polynomials in A_β applied to b; the

Table 2: When fixed-operator ST–MLEE is useful. The symbols are defined in (11)–(13) and should be recomputed for each mesh, tolerance and hardware setting.

Workflow	Reusable object	Cost decision
Dense or analytic basis	Eigensystem of the fixed self-adjoint operator.	Useful when many times, receivers or dense source weights share the same operator and $q \geq q_*$ at matched accuracy.
Sparse Lanczos action	Krylov basis generated from the fixed operator and starting source vector.	Useful for repeated receiver-time queries for that source; source changes require rebuild, block Krylov or recycling Krylov.
One-shot or changing model	No reusable representation across the query set.	Time marching may be cheaper when setup cannot be amortised or when non-self-adjoint boundaries require another matrix-function method.

Ritz space therefore reflects the spectral measure induced by that source. Moving the source changes the modal weights and can leave the old basis poorly aligned with the new response. With $m = 120$, source A on its own basis differs from an $m = 160$ reference by 1.47%. Forcing a shifted source B through source A's basis raises the receiver-waveform error to 270%; rebuilding the basis from source B reduces the error to 1.26% (Figure 8a). A source-perturbation scan with $\eta_b = \|b_\delta - b_A\|/\|b_A\|$ first exceeds the 1.5% tolerance at $\eta_b = 0.015$. Rebuilding the source-specific basis keeps the error between 0.78% and 1.48% throughout the scan (Figure 8b).

Fast convolution, sum-of-exponentials and rational-memory schemes accelerate the history-dependent Caputo convolution while still advancing through intermediate times. ST–MLEE instead evaluates a matrix function of the fixed self-adjoint operator at the requested times. Optimized history compression remains the relevant comparison when an application needs every intermediate time step or changes the operator between trials. Operational regimes and reuse boundaries for modal and Lanczos pathways are compiled in Table 2.

3.2 Evaluating the Mittag-Leffler function

The modal factors require accurate values of $E_\alpha(-s)$ for $1 < \alpha < 2$ over the full range $s = \mu_n t^\alpha$. For small to moderate $|s|$ we sum the defining series with Kahan compensation; for large $|s|$ the series becomes strongly cancelling and we switch to the asymptotic expansion. For $1 < \alpha < 2$ the asymptotics include an *oscillatory* contribution from the complex conjugate pair of α-th roots,

$$E_{\alpha,\nu}(-s) \sim \frac{2}{\alpha}\, s^{(1-\nu)/\alpha} e^{\rho\cos\vartheta} \cos\big(\rho\sin\vartheta + \vartheta(1-\nu)\big) - \sum_{k=1}^{K} \frac{(-1)^k s^{-k}}{\Gamma(\nu-\alpha k)}, \qquad \rho = s^{1/\alpha},\ \vartheta = \frac{\pi}{\alpha}, \tag{14}$$

($\nu = 1$ for $E_\alpha = E_{\alpha,1}$). This is the large-s asymptotic on the positive real s-axis used by the modal factors $-\mu_n t^\alpha$; it is invoked only after the algebraic terms decrease under the selected tolerance. Since $\cos(\pi/\alpha) < 0$ for $1 < \alpha < 2$, the displayed oscillatory exponential is damped as $s \to \infty$. The symbol ν is the second Mittag–Leffler parameter and is unrelated to the spatial order β. Omitting the oscillatory term turns the algebraic decay into a spurious monotone one and corrupts both the dispersion slope and the constant-Q test. In the implementation used here, the series/asymptotic crossover is chosen after comparison with high-precision (`mpmath`) reference values.

The only approximation in (10), once E_α is evaluated to round-off, is the truncation of the eigenmode sum to M modes. For $1 < \alpha < 2$ the Mittag-Leffler kernel is bounded, $|E_\alpha(-\mu_n t^\alpha)| \leq C_\alpha/(1 + \mu_n t^\alpha)$ (Gorenflo et al., 2014), so the tail of (10) is controlled by the regularity of the initial data through its spectral coefficients $a_n = \langle u_0, \phi_n \rangle$.

Proposition 1. *Let $u_0 \in H^s(\Omega)$ for some $s > 0$, with $|a_n| \leq C n^{-(1+2s/d)/2}$ in d spatial dimensions (Weyl asymptotics $\lambda_n \sim n^{2/d}$), and let u_M be the M-mode truncation of (10). Then*

$$\sup_{t\geq 0} \|u(\cdot,t) - u_M(\cdot,t)\|_{L^2(\Omega)} \;\leq\; C_\alpha \Big(\sum_{n>M} |a_n|^2 \Big)^{1/2} \;\leq\; C'\, M^{-s/d}, \tag{15}$$

i.e. the truncation error decays algebraically at a rate set by the smoothness of the source, uniformly in time.

Proof. Orthonormality of $\{\phi_n\}$ and the uniform bound $|E_\alpha(-\mu_n t^\alpha)| \leq C_\alpha$ give $\|u - u_M\|_{L^2}^2 = \sum_{n>M} |a_n|^2 |E_\alpha(-\mu_n t^\alpha)|^2 \leq C_\alpha^2 \sum_{n>M} |a_n|^2$; substituting the decay of a_n and comparing with an integral yields the $M^{-s/d}$ rate. $\square$

The algebraic decay rate $M^{-s/d}$ in Proposition 1 ties modal truncation to the Sobolev regularity of the initial wavefield. The Gaussian source weights used in the experiments suppress Gibbs ringing from high modes. A singular point source does not satisfy the $s > 0$ assumption in two or three spatial dimensions, so the algebraic bound (15) should not be applied to an unsmoothed Dirac load. Such a source would require mollification, receiver averaging or a larger retained modal space, with the corresponding cost included in T_{setup} or T_{cached}.

4 Constant order: same-equation validation and diagnostic suite

We validate the constant-order ST–MLEE through analytic limits, spatial-operator convergence, an independently assembled FEM and complete receiver-waveform benchmarks. The 2-D/3-D comparison changes the temporal evaluator while retaining the same semidiscrete Dirichlet operator. Heterogeneous and field-informed examples are used after these benchmark validations as application-scale illustrations.

The modal-response diagnostic measures Q from half-power bandwidth across the tested band. The measured Q is frequency-flat within numerical tolerance, confirming the constant-Q property (8).

Figure 5 fits the phase velocity $v_p \propto \omega^\gamma$ from the oscillation frequency of two-station responses; the fitted γ follows the predicted value $1 - \alpha/\beta$ across the tested range of (α, β).

The classical-limit diagnostic takes $\alpha \to 2$ at fixed $\beta = 2$. In this limit the attenuation vanishes and the ST–MLEE solution converges to the loss-free wave solution.

4.1 Positive self-adjoint spectral-operator verification

We constructed the Dirichlet finite-difference Laplacian at $N = 24, 48, 96, 192$ and formed its spectral fractional power for $\beta = 1.6$. At $N = 192$ the relative symmetry defect was 1.50×10^{-16}, the minimum eigenvalue was positive (6.24), and the first fractional eigenvalue differed from its analytic sine-basis value by 1.77×10^{-5}. These values confirm positivity, self-adjointness and spatial convergence for the spectral discretisation. This controlled check isolates the operator construction; the independent FEM and matched receiver-waveform tests below address discretisation independence and end-to-end accuracy.

4.2 Independent discretisation checks

A consistent-mass linear FEM generalized eigenproblem, assembled independently of the finite-difference spectral matrix, converged at second order: the first fractional eigenvalue error decreased from 2.57×10^{-3} (16 elements) to 1.00×10^{-5} (256 elements). For the smooth periodic variable-β family, nested-grid refinement reduced the operator-action difference from 4.17×10^{-3} to 1.01×10^{-11} and the propagated-field difference from 6.63×10^{-5} to 2.73×10^{-12}. The smooth declared family was therefore reproduced across nested grids. On the 14,598-cell irregular grid,

$m = 120$ and $m = 160$ gave 1.445% and 0.237% receiver errors relative to an extended $m = 240$ Lanczos reference. Finally, a non-shared two-dimensional classical-limit test compares discrete-sine modal evolution with direct leapfrog time marching on a separate 192^2 grid; the receiver difference decreases from 14.60% at 24^2 to 0.90% at 96^2. This last result is used as an elastic-limit check for $(\alpha, \beta) = (2, 2)$. Fractional-wave cross-model validation is discussed in Section 6.

4.3 Complete 2-D and small 3-D matched-accuracy wavefield benchmark

We benchmark complete receiver waveforms rather than scalar temporal kernels. All methods use the same Dirichlet finite-difference Laplacian, smooth initial wavefield, three receivers, 24 output times on $[0, 0.55]$, and $(\alpha, \beta) = (1.72, 1.80)$. The two grids contain 64^2 and 26^3 unknowns. The 26^3 case tests the three-dimensional implementation at a controlled verification scale. ST–MLEE evaluates the modal Mittag–Leffler evolution directly; the independent controls are the velocity-form L1 method and a Caputo-corrected Grunwald–Letnikov (GL) history method at three time steps. Each timing is the median of three CPU runs on an Intel64 Family 6 Model 183 processor; the installed RTX 5070 was not used. No OpenMP, MKL, OpenBLAS or NumExpr thread-count variable was set in the review run. Incremental peak resident memory was sampled at 2 ms. The spectral route has Krylov dimension zero and scalar Mittag–Leffler tolerance 10^{-12}; the history methods use direct diagonal modal solves.

Both history methods converge under step halving toward the direct modal ST–MLEE solution of the same semidiscrete fractional equation. At the prespecified 1.5% receiver waveform-error tolerance, the 2-D L1 and GL runs require $\Delta t = 0.00275$, take 0.15 s, and add approximately 6.3 MiB of resident memory, while ST–MLEE takes 0.15 s and adds less than 0.6 MiB. In 3-D, the matched L1 and GL runs take 0.24–0.25 s and add 26.8–26.9 MiB; ST–MLEE takes 0.22 s with no time-history array. The nested local $\beta = 2$ control is faster but has 20.5% and 34.5% waveform error and is therefore excluded from the matched-accuracy ranking. Figure 6 reports the runtime–error and memory comparison against this direct-modal reference for these self-adjoint grids. Production-scale 3-D and GPU extensions are discussed in Section 6.

These comparisons keep the semidiscrete fractional equation fixed. ST–MLEE, L1 and GL differ in the temporal evaluator, so the waveform errors isolate the requested-time calculation rather than a change of physical model.

Table 3: Independent same-equation checks for the complete-wavefield tests. All rows use the same fractional equation and the same self-adjoint Dirichlet operator as the ST–MLEE run being tested.

Test	Equation and operator	Independent part	Error metric	Pass tolerance
2-D receiver waveforms	$(\alpha,\beta) = (1.72, 1.80)$ on 64^2 Dirichlet grid	Velocity-form L1 and Caputo-corrected GL histories	Three-receiver waveform discrepancy at 24 output times	Both history controls below 1.5% at the matched step.
3-D receiver waveforms	Same fractional equation on 26^3 Dirichlet grid	Independently coded L1/GL time histories	Same receiver waveform metric and output schedule	Both history controls below 1.5%; ST–MLEE stores no time-history array.
Classical limit	$(\alpha,\beta) = (2,2)$ on a separate sine-grid sequence	Direct leapfrog time marching	Receiver discrepancy under grid refinement	Reaches 0.90% at 96^2 versus 192^2; used only as an elastic-limit check.

4.4 Sparse Krylov test on an irregular heterogeneous operator

The preceding matched benchmark uses an analytic sine basis and therefore does not test the sparse route in the solver hierarchy. We form the symmetric positive five-point operator $-\nabla\cdot(c^2\nabla)+0.02I$ on an irregular active-cell domain with a wavy top boundary, a Dirichlet notch, smooth layering, a high-velocity dome and a low-velocity dipping fault zone. A single-source matrix Mittag–Leffler action is approximated by Lanczos projection; the projected tridiagonal matrix is diagonalised once and reused at 13 output times and four receivers for that same starting vector. This is the sparse matrix-action route used in the source-dependence tests below.

Four grids from 32^2 to 128^2 contain 915, 3,648, 8,211 and 14,598 active cells. For each grid, Krylov dimensions 40, 80, 120 and 160 are nested in the same Lanczos run, and the $m = 160$ receiver traces provide the original internal projection reference. At $m = 120$ the relative receiver-waveform errors are 8.3×10^{-8}, 6.5×10^{-6}, 0.593% and 1.466%, respectively, so every grid meets the 1.5% waveform tolerance. On the largest grid the measured CPU build-plus-evaluation time is 0.18 s and the stored sparse operator plus Krylov basis is 14.4 MiB (Figure 7). An extended $m = 240$ calculation checks the projection truncation level within the same algorithm. Extensions to multi-source block Krylov, GPU kernels, field-scale meshes and absorbing boundaries are discussed in Section 6. The test measures stability of the fixed-operator matrix-function route on an irregular positive operator and agreement with a larger Lanczos reference.

The main validation grids use symmetric positive semidiscrete operators, so the modal theorem and the matched L1/GL controls refer to the same self-adjoint object. Sponge layers appear only in auxiliary effective-medium controls to suppress late boundary reflections in diagnostic wavefield runs. Production absorbing boundaries that enter the operator itself are treated as extensions in the Discussion.

For the largest tested grid, $m = 120$ is the economical screening choice because it meets the 1.5% waveform tolerance. The $m = 160$ basis is the preferred reporting choice when the discrepancy must remain below 0.25% relative to the extended $m = 240$ calculation. On a new operator, m should be increased until consecutive projected receiver traces and a higher-dimensional reference satisfy the application tolerance. Memory and timing should then be reported for that selected dimension.

A sparse-history timing check was also run on the largest irregular operator. For the $m = 120$ Lanczos route, $T_{\text{setup}} = 0.124$ s and $T_{\text{cached}} = 9.43 \times 10^{-3}$ s per 13-time, four-receiver query batch. The finest tested implicit L1 march used $dt = 5 \times 10^{-4}$, 1041 time levels and $T_{\text{hist}} = 13.0$ s per batch after factorisation. This gives $q^*_{\text{sparse}} = 1$ for this timing check. The same L1 march remained at 5.43% receiver error relative to the $m = 160$ Krylov reference, above the 1.5% tolerance; matched-accuracy sparse-route break-even values therefore require a history, contour or higher-dimensional reference baseline at the same receiver-waveform tolerance.

After the complete matched-waveform tests, Figure 4 provides a narrower temporal-kernel comparison against a convergent $L1$ finite-difference discretisation of (2). On the analytic-eigenbasis problem used there, ST–MLEE attains the reference tolerance at lower temporal cost and without stored history, with the gap widening as the $L1$ scheme pays its $O(N_t^2)$ history convolution. Figure 4 isolates the temporal-kernel cost, whereas the 2-D/3-D benchmarks above compare complete receiver waveforms at matched accuracy.

4.5 Application to heterogeneous seismic models

Analytic or manufactured geometries separate spatial and temporal errors; heterogeneous models test exact-in-time evaluation after a seismic operator has been assembled. The self-adjoint setting is the spectral fractional Laplacian or an operator generated by a symmetric positive form.

For a heterogeneous *velocity* $c(\mathbf{x})$, the spatial operator remains self-adjoint (e.g. $\mathcal{A} = -\nabla \cdot (c^2 \nabla)$), so it retains a discrete orthonormal eigenbasis and the ST–MLEE diagonalisation is preserved: the analytic (sine/Fourier) eigenpairs are replaced by the *numerical* eigenpairs of $\mathcal{A}$, and the direct modal evaluation goes through unchanged. A spatially varying *order* requires a specified semidiscrete operator and is treated separately in §5; the same heterogeneous-velocity eigenbasis mechanism recurs in the field-data forward reported in Supplementary Material S2. Figure 9 demonstrates the fixed-operator formulation on a heterogeneous salt-dome velocity structure using the numerical eigenbasis of the heterogeneous operator. Quantitative accuracy and memory comparisons are reported separately in the same-equation benchmarks.

4.6 Supporting effective-medium context

We treat β as an effective nonlocal-dispersion coordinate rather than assuming a specific fractal closure. Supporting full-wave calculations through lossless fractal random media show apparent scattering attenuation but do not support the simple $\beta = 3 - D_f$ closure in the tested transmission and near-source geometries. The benchmarks below therefore use β as an effective order in the semidiscrete operator, rather than as a calibrated microstructural law.

5 Variable-space-order semidiscrete operator

The fixed-operator argument extends to spatially varying $\beta(\mathbf{x})$ only after a symmetric positive semidiscrete matrix has been defined. For constant α, that matrix has an orthonormal eigenbasis and evolves mode-wise through the same Mittag–Leffler kernel. The tests below therefore concern the projected matrix used in the computation, not a universal discretisation of every continuous variable-order fractional Laplacian. Smooth nested-grid checks show where this construction behaves regularly. A discontinuous-order counterexample marks the point where explicit interface treatment becomes necessary.

5.1 Variable space order $\beta(\mathbf{x})$: time-continuous modal evaluation

When only the space order varies (constant α), the time dependence can be represented without time discretisation after the spatial operator has been fixed. We prescribe $S_h[\beta] = \frac{1}{2}\{A_h[\beta] + A_h[\beta]^*\}$, where $A_h[\beta]$ is the discrete Kohn–Nirenberg quantisation of the grid symbol $c^2|\xi|^{\beta(\mathbf{x})}$

under the bounded-domain convention used in the code. This construction makes S_h real symmetric and reproduces the discrete Fourier multiplier for constant β; symmetry alone does not guarantee positivity. The unprojected symmetrisation is not non-negative: the reproducible check finds one eigenvalue of -2.1334×10^{-3} at each of $N = 24, 48, 96$ for the smooth contrast test. We therefore define the stable semidiscrete operator as the spectral projection $L_h = S_h^+ = \Psi \max(\Lambda, 0)\Psi^*$. This numerical regularisation is adopted for the present variable-order experiment. It fixes a positive self-adjoint matrix on which the Mittag–Leffler evolution is well defined, but it is not a continuum variable-order fractional Laplacian and does not impose a physical interface condition. For smooth $\beta(\mathbf{x})$, the projection is a minor correction in the tested matrix sequence. For discontinuous β, the method is not recommended without additional interface regularisation or transmission conditions (Section 6.1). Let $(\widehat{\lambda}_n, \psi_n)$ be its numerical eigenpairs. Projecting ${}^{C}D_t^{\alpha} u + Lu = 0$ onto ψ_n gives, per mode, a constant-order scalar Caputo equation, so

$$u(\mathbf{x}, t) = \sum_n \langle u_0, \psi_n \rangle \, E_\alpha(-\widehat{\lambda}_n t^\alpha) \, \psi_n(\mathbf{x}), \tag{16}$$

which is (10) with the numerical eigenbasis of L in place of the Laplacian eigenbasis. The evaluation is time-continuous at the semidiscrete level and is made directly at requested times. It imposes no perturbative restriction on the amplitude of the β-variation for the projected matrix. Against an independently implemented constant-α $L1$ time march of the same operator L, the modal ST–MLEE evaluation (16) reproduces the field to the reference's time-discretisation floor for the projected operator, holding at $\beta(\mathbf{x}) \in [0.76, 1.98]$. A naive weak-variation perturbation is included for reference and its error grows with contrast. Refining the reference time step drives the $L1$ solution toward (16), confirming that the modal Mittag–Leffler evaluation is the time-continuous limit of the semidiscrete system. Smooth variable $\beta(\mathbf{x})$ therefore does not reintroduce stored Caputo history once the matrix model has been fixed. A four-grid check ($N = 24, 48, 96, 192$) clarifies the numerical scope. For the smooth periodic order profile, the relative PSD correction decreases from 1.37×10^{-5} to 1.24×10^{-7} and the projected fields differ from the $N = 192$ field by at most 1.52×10^{-9} on the coarser nested grids. For a discontinuous step in β, however, the unprojected minimum eigenvalue grows in magnitude from -0.35 to -95.7, the relative PSD correction increases from 1.92×10^{-3} to 5.17×10^{-3}, and the field differences decrease only from 9.33% ($N = 24$) to 2.85% ($N = 96$). Hence the smooth test supports consistency of this discrete sequence for smooth data, whereas the step test does not support a general continuous–discrete consistency claim. A directional perturbation check of the projected map gives relative first-order remainders $0.0103, 0.0204, 0.0399, 0.0766$ and 0.1427 for contrasts $0.02, 0.04, 0.08, 0.16, 0.32$, respectively. These values are consistent with a locally differentiable map but not a global perturbative approximation. For discontinuous order jumps, the projection S_h^+ may remove or alter interface-localized components of the symmetrized Kohn–Nirenberg matrix. Sharp geological interfaces therefore require the additional interface treatment discussed in Section 6, such as explicit transmission conditions, a finite regularization length or a nonlocal jump formulation. An independent periodic singular-integral quadrature, which does not reuse the Kohn–Nirenberg matrix, gives relative operator-action differences 0.459, 0.392 and 0.338 and propagated-field differences 0.311, 0.254 and 0.211 on $N = 32, 64, 128$. The differences decrease but do not establish a common limit at these resolutions. This definition-sensitivity check is included in the Supplementary Material, together with the shared smooth two-dimensional low-Q anomaly diagnostic.

5.2 Additional variable-order extensions

Jointly variable temporal and spatial orders do not admit one fixed modal evolution, because the pointwise temporal order does not commute with spatial projection. The corresponding Laplace–Talbot/Bromwich formulation, its synthetic tests, the Cranfield closed-loop illustration and the relaxation-order superposition are provided in the supplementary material. They avoid stored time histories but require independent contour-node solves or multiple modal responses, so their setup and reuse costs differ from the fixed-operator setting established here.

5.3 Measured fixed-operator reuse crossover

Cached reuse was tested separately with modal weights and an independently implemented L1 history solver on the same 26×26 Dirichlet operator. The L1 step 7.5×10^{-4} stores 561 history states per source and yields mean receiver discrepancies of 0.17–0.78% across one to 16 smooth source queries. Including the 0.0198 s modal-weight setup, the cached spectral totals are 0.0200–0.0226 s, whereas the L1 totals grow from 0.0477 to 0.788 s (Figure 3); the spectral evaluator stores no preceding time states. These CPU timings isolate the fixed-operator repeated-query mechanism and include the modal-weight setup, but not a general eigendecomposition, GPU, absorbing boundary or production mesh. In this analytic-basis benchmark the measured setup is 0.0198 s and the one-source L1 total already exceeds the cached spectral total (0.0477 versus 0.0200 s), so (11) gives $q_* = 1$ for this low-setup small problem. Because each history solve stores 561 preceding states while the cached spectral evaluator stores none, the same data also illustrate the requested-time sparsity accounting of (12); applications that need only selected receiver times should recompute ρ_t and q_* for the target output schedule. The reported crossover should not be transferred to a heterogeneous mesh without charging the new setup cost.

6 Discussion

Within the tested operator class, requested-time evaluation can be separated from time marching. Dense modal evaluation is useful when an eigendecomposition can be amortised across times, receivers and source weights. Sparse Lanczos projection provides the tested source-dependent matrix-action route on an irregular grid. The matched same-equation receiver tests in Table 3 and the extended Krylov reference quantify accuracy in those cases, while the memory comparison concerns the recorded time-history array rather than total solver memory.

Existing variable-order finite-difference and Fourier pseudospectral schemes (O et al., 2024; Zhang et al., 2026) treat broader time-marching settings. The present tests address a narrower question: when a self-adjoint semidiscrete operator is fixed, can selected seismic responses be evaluated more naturally as matrix-function queries? The fixed-operator response queries are governed by T_{setup}, ρ_t and ρ_r, rather than by the scalar cost of a single Mittag–Leffler evaluation. Typical batches include sparse-time waveform extraction, multi-source weight sweeps, receiver-aperture tests, fixed-operator uncertainty quantification and synthetic benchmarks for history algorithms. A standard FWI outer loop changes the operator after each model update; the accounting must then be restarted inside each fixed-operator batch unless a Krylov recycling strategy is introduced.

The companion continuous-operator analysis (Hu et al., 2025) supplies the branch-resolved attenuation–dispersion interpretation of the two-order model. Here the emphasis is numerical: same-equation receiver traces, memory and setup amortisation are compared for the semidiscrete operators actually evaluated.

6.1 Limitations and scope

The irregular-grid source test gives the sharpest reuse boundary: standard single-vector Lanczos reuse is source-specific. On the largest irregular operator, reusing the source-A basis after an $\eta_b = 0.015$ source perturbation already exceeds the 1.5% waveform tolerance. Multi-source seismic workflows therefore require a different sparse route. A block Krylov extension would build

$$K_m(A,B) = \mathrm{span}\{B, AB, \ldots, A^{m-1}B\}, \qquad B = [b_1, \ldots, b_{N_s}],$$

and would replace (11) by

$$q_*^{\mathrm{block}} = \left\lceil \frac{T_{\mathrm{setup}}^{\mathrm{block}}}{N_s T_{\mathrm{hist}} - T_{\mathrm{cached}}^{\mathrm{block}}} \right\rceil, \qquad N_s T_{\mathrm{hist}} > T_{\mathrm{cached}}^{\mathrm{block}},$$

when a query batch contains N_s sources. This route is attractive only when the block rank remains moderate. Without rank compression, m block steps may store up to mN_s basis vectors. Memory then scales as $O(N_{\mathrm{dof}} m N_s)$, the orthogonalisation cost rises with block size, and the projected matrix function has dimension mN_s. In FWI-style multi-shot settings with many nearly independent sources, recycling or deflated restarted Krylov methods are more plausible than a large monolithic block basis. They retain a smaller subspace and enrich it only where the previous basis remains useful. Both alternatives require a fresh measured q_*, because source batching changes setup cost, cached-query cost and the waveform-error curve.

The variable-β experiment defines a positive semidiscrete matrix before time evolution is applied. Smooth nested-grid agreement supports that discrete sequence, but discontinuous-order and independent-integral tests do not define a general continuous variable-order operator. At geological contacts, the PSD projection acts as a stabilizing positive filter on the chosen matrix representation. It can remove interface-localized negative components, but it does not impose displacement, stress or nonlocal flux continuity. A field-ready interface model would need a bandwidth-dependent smoothing length ℓ_{reg}, an explicit transmission condition or a nonlocal jump formulation.

PML and complex stretched-coordinate absorbing layers usually produce non-self-adjoint operators (Komatitsch & Martin, 2007). A complex-frequency-shifted PML would move the problem outside the orthogonal spectral representation used here. Extension to such 3-D production models would require sectorial or non-normal matrix-function techniques, including contour-integral and rational Krylov methods (Higham, 2008; Weideman & Trefethen, 2007; Moret, 2015; Danczul et al., 2023). The orthogonal modal basis and symmetric Lanczos error indicators would be replaced by non-normal resolvent behaviour, possible pseudospectral sensitivity and shifted linear solves at contour or rational poles. The break-even count q_* would then include factorisations or preconditioners for those shifted systems and must be remeasured for that solver class.

The constant-order $L1$/GL checks are independent time-discretisation implementations of the same fixed semidiscrete fractional evolution, and the refined-grid leapfrog comparison reaches 0.90% only in the classical $(\alpha, \beta) = (2, 2)$ limit. A comparison with an independently implemented k-Wave fractional solver is included in Supplementary Material S3; it tests a different governing equation and is therefore not part of the validation hierarchy.

7 Conclusions

Selected responses of fixed fractional-seismic operators need not be obtained by a complete Caputo history march. For a positive self-adjoint semidiscrete operator A_β, the queried datum is

$$d_r(t) = r^T E_\alpha(-t^\alpha A_\beta)b,$$

and the relevant reporting quantities are the setup cost, cached query cost, requested-time fraction and receiver sparsity.

Dense-modal and Krylov implementations pass same-equation checks against independent FEM assembly and L1/GL time-stepping controls at the tested scales. On the largest irregular grid (14,598 active cells), $m = 120$ differs from an extended 240-vector Lanczos reference by 1.445%, and $m = 160$ reduces the discrepancy to 0.237%. Single-vector Lanczos reuse is source-specific. Shifting the source while reusing the old basis raises the receiver error by more than two orders of magnitude, while rebuilding the source-specific basis restores the 1–2% level. A source-perturbation scan places the first 1.5%-tolerance failure at $\eta_b = 0.015$. The same irregular operator gives a diagnostic $q^*_{\text{sparse}} = 1$ against the fastest tested L1 march, with that baseline remaining above the matched waveform-error tolerance.

For a smooth variable-space-order matrix, nested-grid operator-action and propagated field differences decrease to near round-off. Discontinuous-order and cross-definition checks show where an additional interface law is needed. Dense eigenbasis reuse and source-dependent Lanczos actions must be kept separate, and operator-changing workflows must rebuild the representation. For fixed fractional seismic operators, selected receiver-time responses become reusable matrix-function queries once the number of queries is large enough to amortise setup. Non-self-adjoint absorbing boundaries require contour-integral, rational Krylov or related non-normal matrix-function formulations.

Data Availability

Two published/public datasets are used. The rock-physics motivation in the Supplementary Material replots the Table-1 median values of Sams et al. (1997) (doi:10.1190/1.1444249). The supplementary real-data demonstration uses the public Denbury/LBNL Cranfield 3-D VSP (SECARB Phase III, well CFU 31F #1), including raw true-amplitude SEG-Y shot records, geometry and the supplied first-break pick file. All other results are synthetic.

The reproducibility archive supplied with this submission contains the ST–MLEE implementations, history-solver controls, irregular-grid Krylov tests, source-dependence scans, variable-order diagnostics, supplementary figures and all machine-readable CSV/JSON outputs. The code and source data for the reported validation and diagnostic results are archived on Zenodo at `https://doi.org/10.5281/zenodo.21486072`. The review environment used Python 3.12 with `numpy` 2.5.1, `scipy` 1.16.3 and `matplotlib` 3.10.7. Timing runs are CPU-only; strict single-thread reruns may set `OMP_NUM_THREADS=1`, `OPENBLAS_NUM_THREADS=1`, `MKL_NUM_THREADS=1` and `NUMEXPR_NUM_THREADS=1`. The double-anonymous review archive removes author-identifying paths and includes deterministic run commands for every table and figure.

References

Aki, K., Richards, P.G., 1980. *Quantitative Seismology: Theory and Methods*. W.H. Freeman, San Francisco.

Abate, J., Valkó, P.P., 2004. Multi-precision Laplace transform inversion. *Int. J. Numer. Methods Eng.* **60**, 979–993, doi:10.1002/nme.995.

Bazhlekova, E., 2001. *Fractional Evolution Equations in Banach Spaces*. PhD thesis, Eindhoven University of Technology.

Blanch, J.O., Robertsson, J.O.A., Symes, W.W., 1995. Modeling of a constant Q: methodology and algorithm for an efficient and optimally inexpensive viscoelastic technique. *Geophysics* **60**, 176–184, doi:10.1190/1.1443744.

Caputo, M., Mainardi, F., 1971. Linear models of dissipation in anelastic solids. *La Rivista del Nuovo Cimento* **1**, 161–198, doi:10.1007/BF02820620.

Carcione, J.M., 2014. *Wave Fields in Real Media: Theory and Numerical Simulation of Wave Propagation in Anisotropic, Anelastic, Porous and Electromagnetic Media*, 3rd edn. Elsevier, Amsterdam.

Chen, W., Holm, S., 2004. Fractional Laplacian time–space models for linear and nonlinear lossy media exhibiting arbitrary frequency power-law dependency. *J. Acoust. Soc. Am.* **115**, 1424–1430, doi:10.1121/1.1646399.

Danczul, T., Hofreither, C., Schöberl, J., 2023. A unified rational Krylov method for elliptic and parabolic fractional diffusion problems. *Numer. Linear Algebra Appl.* **30**, e2477, doi:10.1002/nla.2477.

Gorenflo, R., Kilbas, A.A., Mainardi, F., Rogosin, S.V., 2014. *Mittag-Leffler Functions, Related Topics and Applications*. Springer, Berlin, doi:10.1007/978-3-662-43930-2.

Garrappa, R., Moret, I., Popolizio, M., 2015. Solving the time-fractional Schrödinger equation by Krylov projection methods. *J. Comput. Phys.* **293**, 115–134, doi:10.1016/j.jcp.2014.10.051.

Higham, N.J., 2008. *Functions of Matrices: Theory and Computation*. SIAM, Philadelphia, doi:10.1137/1.9780898717778.

Hu, N., Li, S., Huang, C., Sun, J., 2025. Branch-resolved fixed-band near-constant-Q criteria for variable-order fractional seismic attenuation. *EarthArXiv preprint*, doi:10.31223/X53J5R.

Hochbruck, M., Lubich, C., 1997. On Krylov subspace approximations to the matrix exponential operator. *SIAM J. Numer. Anal.* **34**, 1911–1925, doi:10.1137/S0036142995280572.

Holm, S., Näsholm, S.P., 2011. A causal and fractional all-frequency wave equation for lossy media. *J. Acoust. Soc. Am.* **130**, 2195–2202, doi:10.1121/1.3631626.

Kjartansson, E., 1979. Constant-Q wave propagation and attenuation. *J. Geophys. Res. Solid Earth* **84**, 4737–4748, doi:10.1029/JB084iB09p04737.

Komatitsch, D., Martin, R., 2007. An unsplit convolutional perfectly matched layer improved at grazing incidence for the seismic wave equation. *Geophysics* **72**, SM155–SM167, doi:10.1190/1.2757586.

Kwaśnicki, M., 2017. Ten equivalent definitions of the fractional Laplace operator. *Fract. Calc. Appl. Anal.* **20**, 7–51, doi:10.1515/fca-2017-0002.

Lubich, C., 1986. Discretized fractional calculus. *SIAM J. Math. Anal.* **17**, 704–719, doi:10.1137/0517050.

Mainardi, F., 2010. *Fractional Calculus and Waves in Linear Viscoelasticity*. Imperial College Press, London, doi:10.1142/p614.

Moret, I., Novati, P., 2011. On the convergence of Krylov subspace methods for matrix Mittag-Leffler functions. *SIAM J. Numer. Anal.* **49**, 2144–2164, doi:10.1137/100811447.

Moret, I., 2015. A note on the convergence of shift-and-invert Krylov methods for the approximation of the matrix Mittag-Leffler function. *Numer. Funct. Anal. Optim.* **36**, 501–511, doi:10.1080/01630563.2014.985270.

McDonal, F.J., Angona, F.A., Mills, R.L., Sengbush, R.L., Van Nostrand, R.G., White, J.E., 1958. Attenuation of shear and compressional waves in Pierre shale. *Geophysics* **23**, 421–439, doi:10.1190/1.1438489.

Mu, X., Huang, J., Wen, L., Zhuang, S., 2021. Modeling viscoacoustic wave propagation using a new spatial variable-order fractional Laplacian wave equation. *Geophysics* **86**, T487–T507, doi:10.1190/geo2020-0610.1.

Mu, X., Huang, J., Yang, J., Li, Z., Ivan, M.S., 2022. Viscoelastic wave propagation simulation using new spatial variable-order fractional Laplacians. *Bull. Seismol. Soc. Am.* **112**, 48–77, doi:10.1785/0120210099.

Müller, T.M., Gurevich, B., Lebedev, M., 2010. Seismic wave attenuation and dispersion resulting from wave-induced flow in porous rocks—a review. *Geophysics* **75**, 75A147–75A164, doi:10.1190/1.3463417.

Näsholm, S.P., Holm, S., 2013. On a fractional Zener elastic wave equation. *Fract. Calc. Appl. Anal.* **16**, 26–50, doi:10.2478/s13540-013-0003-1.

O'Doherty, R.F., Anstey, N.A., 1971. Reflections on amplitudes. *Geophys. Prospect.* **19**, 430–458, doi:10.1111/j.1365-2478.1971.tb00610.x.

Pride, S.R., Berryman, J.G., Harris, J.M., 2004. Seismic attenuation due to wave-induced flow. *J. Geophys. Res. Solid Earth* **109**, B01201, doi:10.1029/2003JB002639.

Robertsson, J.O.A., Blanch, J.O., Symes, W.W., 1994. Viscoelastic finite-difference modeling. *Geophysics* **59**, 1444–1456, doi:10.1190/1.1443701.

Sams, M.S., Neep, J.P., Worthington, M.H., King, M.S., 1997. The measurement of velocity dispersion and frequency-dependent intrinsic attenuation in sedimentary rocks. *Geophysics* **62**, 1456–1464, doi:10.1190/1.1444249.

Sato, H., Fehler, M.C., Maeda, T., 2012. *Seismic Wave Propagation and Scattering in the Heterogeneous Earth*, 2nd edn. Springer, Berlin, doi:10.1007/978-3-642-23029-5.

Shapiro, S.A., Hubral, P., 1999. *Elastic Waves in Random Media*. Springer, Berlin.

Talbot, A., 1979. The accurate numerical inversion of Laplace transforms. *J. Inst. Math. Appl.* **23**, 97–120, doi:10.1093/imamat/23.1.97.

Treeby, B.E., Cox, B.T., 2010. Modeling power law absorption and dispersion for acoustic propagation using the fractional Laplacian. *J. Acoust. Soc. Am.* **127**, 2741–2748, doi:10.1121/1.3377056.

Wang, Y., 2008. *Seismic Inverse Q Filtering*. Blackwell Publishing, Oxford.

Weideman, J.A.C., Trefethen, L.N., 2007. Parabolic and hyperbolic contours for computing the Bromwich integral. *Math. Comp.* **76**, 1341–1356, doi:10.1090/S0025-5718-07-01945-X.

Winkler, K.W., Nur, A., 1982. Seismic attenuation: effects of pore fluids and frictional-sliding. *Geophysics* **47**, 1–15, doi:10.1190/1.1441276.

Yuan, L., Agrawal, O.P., 2002. A numerical scheme for dynamic systems containing fractional derivatives. *J. Vib. Acoust.* **124**, 321–324, doi:10.1115/1.1448322.

Zhu, T., Carcione, J.M., 2014. Theory and modelling of constant-Q P- and S-waves using fractional spatial derivatives. *Geophys. J. Int.* **196**, 1787–1795, doi:10.1093/gji/ggt483.

O, C.W., Ro, W.M., Kim, Y.C., 2024. An explicit finite difference approximation for space-time Riesz–Caputo variable order fractional wave equation using Hermitian interpolation. *Numer. Anal. Appl.* **17**, 262–275, doi:10.1134/S1995423924030054.

Zhang, Y., Zhao, X., Zhou, S., 2026. Fourier pseudospectral methods for the variable-order space fractional wave equations. *Comput. Phys. Commun.* **318**, 109876, doi:10.1016/j.cpc.2025.109876.

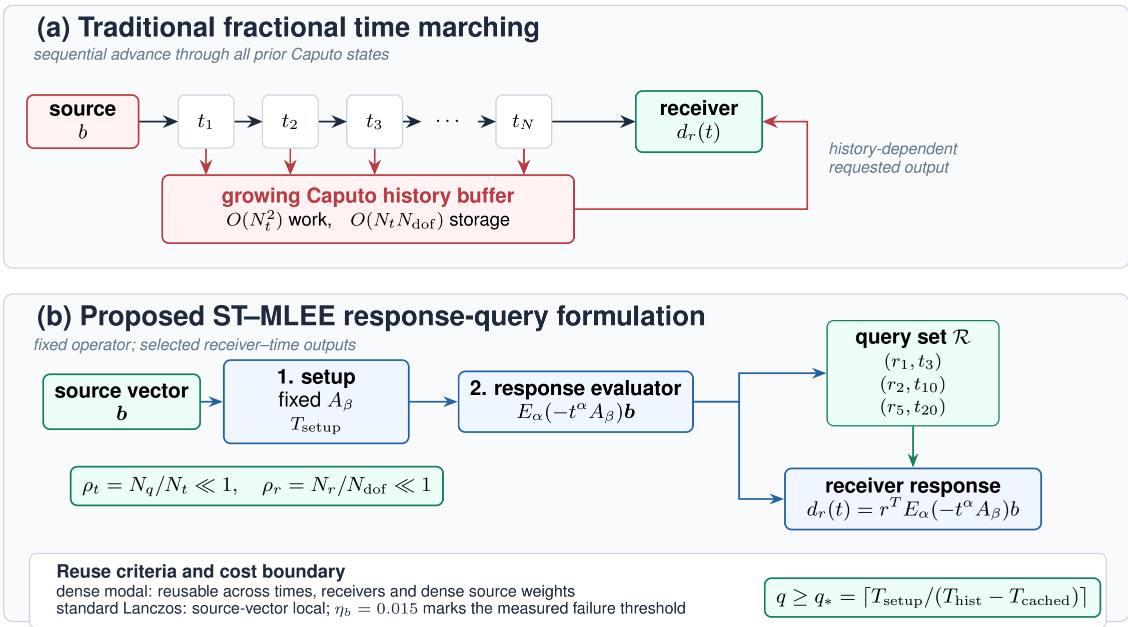

Figure 1: From fractional time marching to requested-response evaluation. Traditional Caputo time stepping advances through all intermediate states and stores or updates the preceding memory before a receiver value at a requested time is available. ST–MLEE fixes the semidiscrete seismic operator A_β once and evaluates selected receiver-time outputs as matrix-function responses. Dense modal bases can be reused across output times, receivers and dense source weights. Standard sparse Lanczos reuse is tied to the starting source vector; changing the source generally requires a new Krylov construction unless block or recycling Krylov methods are introduced. The bottom panel summarizes the operational quantities used later: the requested-time fraction ρ_t, receiver sparsity ρ_r, the measured source-locality threshold η_b, and the matched-accuracy break-even count q_*.

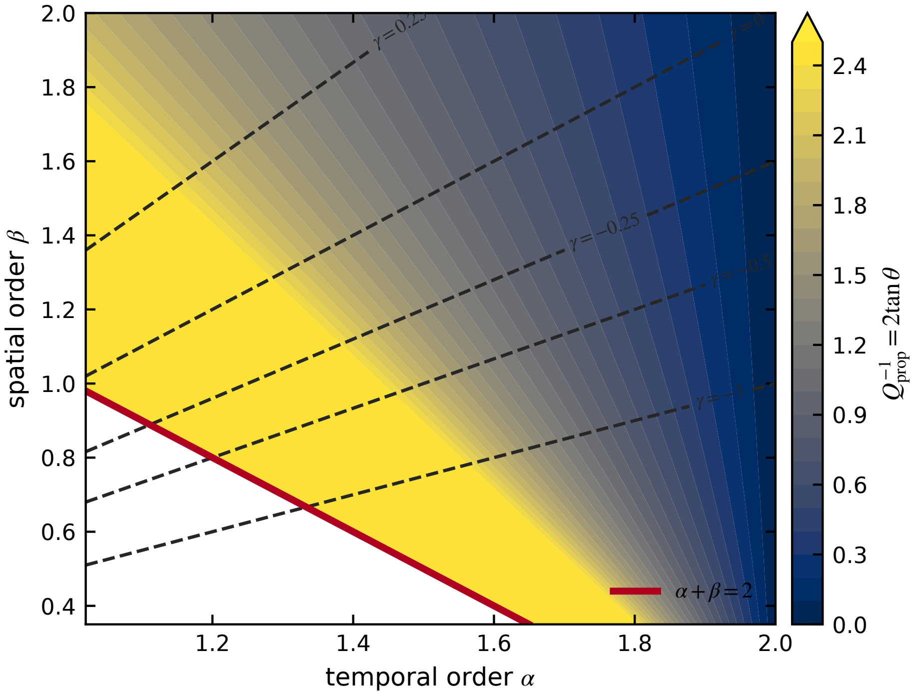

Figure 2: Order-to-observable map. Background colour gives $Q_{\mathrm{prop}}^{-1} = 2\tan\theta$, black dashed curves give $\gamma = 1 - \alpha/\beta$, and the red curve marks the admissibility boundary $\alpha + \beta = 2$. The map shows why attenuation and phase-velocity dispersion must be considered together when interpreting the two fractional orders.

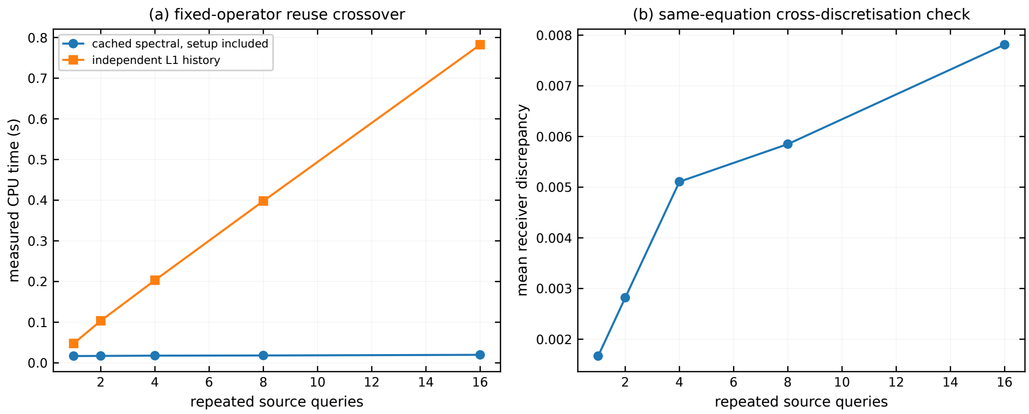

Figure 3: Operational q_* benchmark. (a) Measured cumulative CPU totals for cached fixed-operator requested-response evaluation and an independent L1 history solver on the same Dirichlet operator. The ST–MLEE total has the form $T_{\mathrm{setup}} + qT_{\mathrm{cached}}$, while the history total grows with the number of repeated response queries; the measured crossover is $q_* = 1$ for this low-setup analytic-basis case. (b) Same-equation receiver discrepancy for the refined L1 control. This panel reports setup amortisation for a fixed operator and fixed source-reuse setting; heterogeneous sparse routes require their own matched-tolerance q_*.

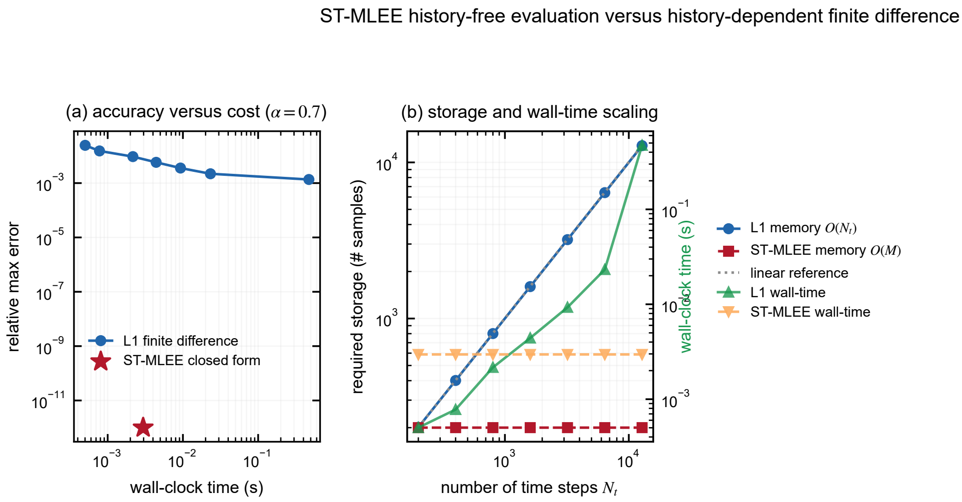

Figure 4: Accuracy/cost benchmark. ST–MLEE reaches reference accuracy against a convergent $L1$ finite-difference scheme while avoiding stored time histories.

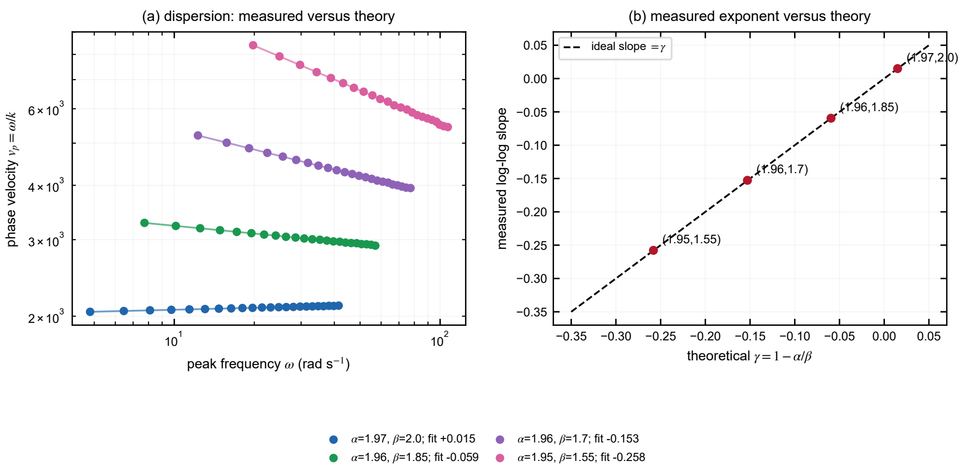

Figure 5: Velocity dispersion. The phase velocity follows $v_p \propto \omega^\gamma$ with $\gamma = 1 - \alpha/\beta$.

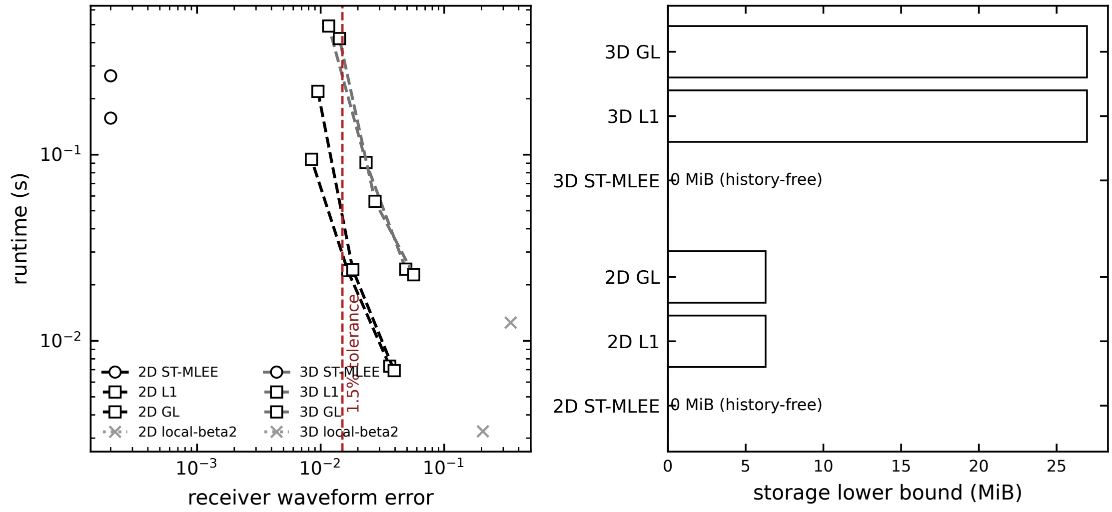

Figure 6: Complete-wavefield matched-accuracy benchmark. Left: runtime versus receiver waveform error measured against the direct modal ST–MLEE solution of the same semidiscrete fractional equation; the dashed red line marks the 1.5% tolerance used for matched-cost comparisons. Right: lower bound on the stored history-array memory for methods passing that tolerance.

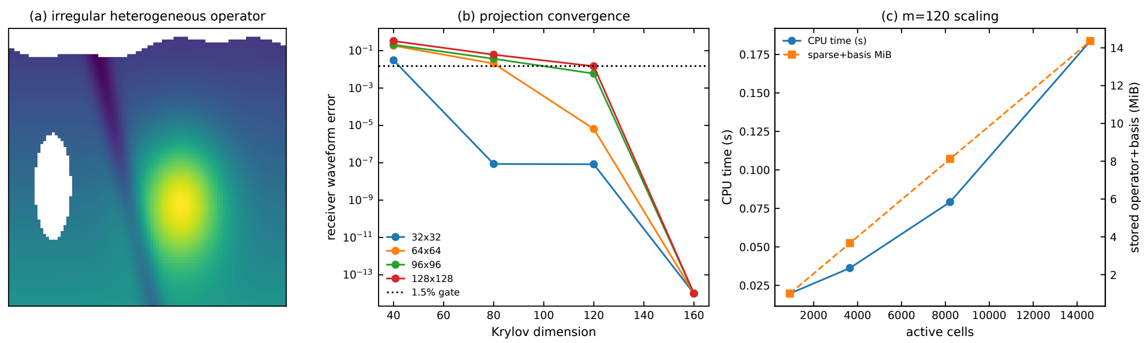

Figure 7: Sparse Krylov test on an irregular heterogeneous operator. (a) Representative active-cell coefficient field. (b) Receiver-waveform convergence to the nested $m = 160$ projection reference; $m = 120$ passes 1.5% on all four grids. (c) Measured CPU time and explicit sparse-operator-plus-basis storage at $m = 120$.

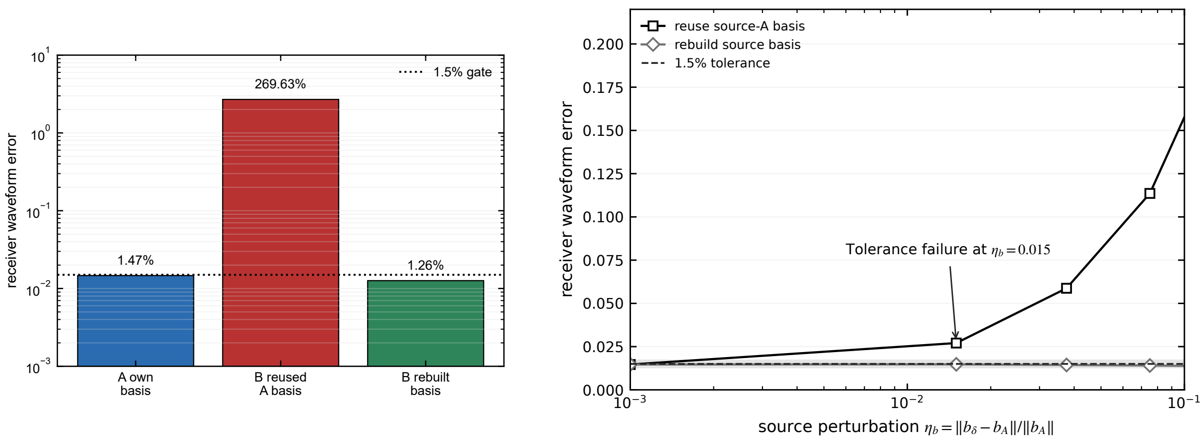

Figure 8: Source locality of standard single-vector Lanczos reuse on the largest irregular heterogeneous operator. (a) With $m = 120$, source A evaluated on its own basis differs from an $m = 160$ reference by 1.47%. Reusing that basis for a shifted source B gives a 270% receiver-waveform error, whereas rebuilding the source-specific basis reduces the error to 1.26%. (b) A perturbation scan reuses the source-A basis while the source centre is moved toward source B. The first 1.5%-tolerance failure occurs at $\eta_b = \|b_\delta - b_A\|/\|b_A\| = 0.015$. Rebuilding the source-specific basis keeps the error near the $m = 120$ truncation level. The threshold measures the locality of the Krylov starting vector, not instability of the underlying fixed-operator matrix function.

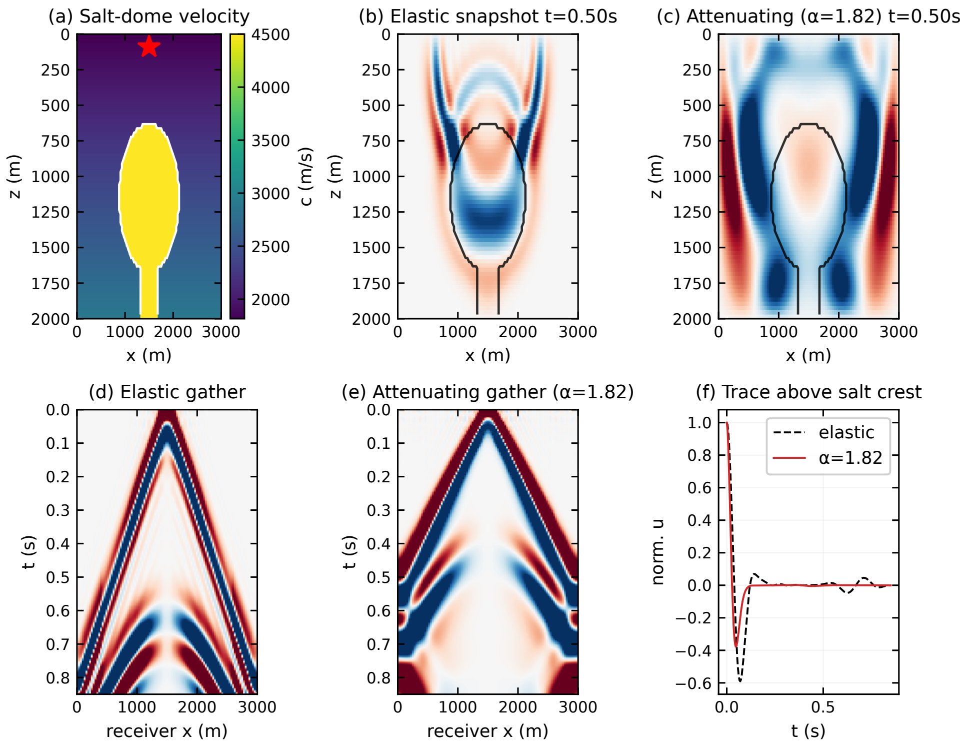

Figure 9: Salt-dome heterogeneous-operator case. ST–MLEE propagation through a salt-dome velocity structure, using the numerical eigenbasis of the heterogeneous operator. The wavefield illustrates requested-response evaluation on a structurally realistic seismic model; quantitative runtime and memory comparisons are reported in the same-equation receiver benchmarks.